
Article:
Liu, B. orcid.org/0000-0002-6840-041X, He, S., Moulinec, C. et al. (1 more author) (2021) Coupled porous media approaches in sub-channel CFD. Nuclear Engineering and Design, 377. 111159. ISSN 0029-5493

https://doi.org/10.1016/j.nucengdes.2021.111159

Coupled Porous Media Approaches in Sub-channel CFD

B. Liu [a,*], S. He [a], C. Moulinec [b] and J. Uribe [c]

[a] Department of Mechanical Engineering, University of Sheffield, Sheffield, S3 7QB, UK

[b] Science and Technology Facilities Council, Daresbury Laboratory, Warrington, WA4 4AD, UK

[c] EDF Energy R&D UK Centre, Manchester, M13 9PL, UK

[*] Correspondence: bo.liu@sheffield.ac.uk

Abstract

In this paper, the porous media method is introduced into a recently developed Computational Fluid Dynamics (CFD)-based sub-channel analysis tool, Sub-Channel CFD (SubChCFD) through direct coupling to improve its capability in modelling complex structures, such as spacers or distorted fuel rod bundles. Two coupling methods have been developed, namely, embedding and interfacing coupling. The former is suitable for rod bundles with attached fine structures which do not change the basic geometry of the sub-channels, so a SubChCFD baseline model can be created based on the bare bundle configuration. Porous media sub-models can then be embedded in this model at locations where fine structures are installed to account for their influence on the flow and pressure drop. The interfacing method is more general and flexible, and used in a wider range of applications. In this method, separate meshes are used for the sub-domains where the porous media method is applied. These sub-domains are then interfaced with the domain covered by SubChCFD using a meshing joining technique and they are simulated together using a single set of governing equations. The methods developed are tested and validated with simulations of two rod bundle configurations, a 7×7 rod bundle with locally ballooned fuel rods and a 5×5 rod bundle equipped with simple support grids. It has been shown that a suitably selected method of the coupling can greatly simplify the modelling of complex structures using SubChCFD, thus providing additional flexibility and functionality to this newly developed CFD-based sub-channel framework.

Keywords

CFD, Coupling, Coarse-grid, Porous media, Nuclear rod bundle, Sub-channel

1. Introduction

Computational Fluid Dynamics (CFD) plays an increasingly prominent role in nuclear reactor thermal hydraulic calculations. It can help the reactor developers to gain better understanding of some important 3-D flow features of the coolants, such as re-circulations, which are difficult to be captured using traditional system/sub-channel codes. However, it is still not feasible to use CFD to perform core-level design calculations and safety relevant analyses for industry due to the prohibitively high computing cost required in resolving the numerous length scales of the flow in a reactor core, despite the remarkable advancement achieved recently in high performance computing techniques (Hanna et al., 2020; Viellieber and Class, 2015). To facilitate the application of CFD in the industry, a hybrid technique, CFD-based sub-channel analysis tool (referred to as Sub-Channel CFD (SubChCFD)), has been proposed in our previous work (Liu et al., 2019), which has proven to be very promising and has a potential to replace or supplement the traditional sub-channel analysis tools.

In essence, SubChCFD is a coarse mesh CFD approach, in which a full set of 3-D conservation equations are solved on a very coarse mesh. The mesh used is usually body-fitted and resolves the main geometry of the flow passages in a fuel assembly (namely the sub-channels), which, for example, consists of only 20 to 40 elements per layer of mesh for a typical interior-type sub-channel in a square lattice Pressurised Water-cooled Reactor (PWR) rod bundle (Liu et al., 2019). This greatly reduces the computing cost compared with conventional CFD. In SubChCFD, the wall effects are accounted for using industry standard sub-channel correlations, ensuring the sub-channel level quantities, such as the wall shear and heat transfer to be reliably calculated for given mass fluxes, the prediction of which is improved by using the 3-D CFD solver. In this view, SubChCFD can be considered as an extension of the traditional sub-channel approaches and allows a higher modelling flexibility than the latter. It is also worth pointing out that the empirical correlations used in closure modelling for the equation system in SubChCFD can be tuned and validated against experimental/industrial data for specific designs of reactors, which ensures consistency in model creation for these reactors and reduces the uncertainty of the predictions.

Despite the drastic reduction in computing cost, the use of a coarse mesh puts some restrictions on the application of SubChCFD. For example, it would be challenging to use SubChCFD for fuel assemblies with complex sub-scale structures (e.g. mixing-vane spacers) that are difficult to be resolved using a coarse mesh. Great caution should also be exercised when the method is used for some off-design reactor conditions where the empirical correlations may be no longer invalid and consequently lead to wrong predictions. To deal with such difficulties, a coupling approach has been developed in our

recent work (Liu et al., 2021), allowing resolved CFD sub-models to be nested into the regions that are of interest but cannot be suitably handled by SubChCFD, to locally improve the prediction. Such a strategy greatly enlarges the application range of SubChCFD but inevitably results in an increase in computing cost, and additionally, the generation of the related refined CFD mesh is usually onerous, tedious and time-consuming. In many cases, reactor designers are mostly interested in some macroscopic behaviours of the flow, such as the global pressure drop, rather than the flow details. In view of this, a simplified treatment of the reactor structures where the detailed flow is of no particular interest will be useful in some practical industry-related applications. Among various candidate solutions, the porous media method is undoubtedly one of the most widely used choices considering its simple formulation and ease of implementation.

Flow through porous media has been studied for more than a century. The early work was mostly based on semi-empirical laws (Darcy, 1856). Recently, more general macroscopic governing equations describing the flow in porous media have been derived rigorously by using a spatial averaging technique (Vafai and Tien, 1981). The microscopic characteristics of the flow at the pore scale are "filtered" out and the associated solid-fluid interactions are accounted for by the new unknown terms that appear during the averaging operation which can be interpreted as the inertial dispersion and interfacial forces (including the friction and the form drag). Closure modelling is usually required for these unknown terms to relate them to the averaged macroscopic flow quantities so that the governing equations can be finally closed. Chandesris et al. (2006) pointed out that the inertial dispersion becomes appreciable only for high speed flows and causes an increase in the form drag, it was therefore suggested to be modelled together with the interfacial forces. For some well-known simple geometries, the closure modelling can be achieved simply through respective pressure loss correlations associated with the wall friction and the form drag.

One of the first attempts of introducing the porous media method into engineering process equipment with complex internal structures was made by Patankar and Spalding (1972) who performed calculations for the flow in the shell side of a heat exchanger where the tube bank was represented using porous media. Such a simplified method greatly reduces the computing cost compared with convectional CFD, as most of the geometrical details are taken into account using porosities rather than being resolved explicitly. Thereafter, the porous media method has been gradually used in various engineering fields, and the nuclear engineering is no exception. Sha et al. (1982) developed a transient, 3-D, thermal hydraulic analysis code based on the porous media method for design purpose calculations of the advanced nuclear heat exchangers. In addition to the volume porosity, they also included the concept of the face permeability in their formulation of the governing equations to

simulate the directional fluid momentum on the shell side of the heat exchanger. Cong et al. (2014) studied the steady thermal-hydraulics characteristics of secondary side of a steam generator in a AP1000 PWR reactor using the porous media method which was implemented in a commercial CFD code ANSYS FLUENT (Ansys Inc., 2011).

The most remarkable success of using the porous media method in 3-D thermal-hydraulics analyses of the nuclear reactor systems is achieved through geometrical simplification of the fuel assemblies in the core, which largely reduces the scale of the computational mesh required and therefore makes the core-scale simulation affordable. For example, Rahimi and Jahanfarnia (2014) performed a thermal-hydraulic analysis of the VVER-1000 reactor core using a porous media approach and the results obtained agreed well with a sub-channel analysis code COBRA-EN. Brewster et al. (2017) simplified their CFD model for a ¼ sector of a 4-loop PWR core using a porous media representation of the fuel assemblies for the centremost section of the core and a mixture of porous media and detailed geometry on the periphery of the core. The mesh size was reduced by more than 90% compared with its CFD counterpart with all geometrical details explicitly modelled. Similar simplification was achieved in the work of Chen et al. (2015) who carried out a coupled CFD/neutron kinetics analysis for a pool type nuclear reactor system. In their CFD model, a porous media model with a physical velocity based pressure loss relation was used to describe the core region of the reactor. Yu et al. (2015) proposed a class of porous models to simulate a wire-wrapped sodium fast reactor fuel assembly. They are two orders of magnitude computationally less expensive than conventional CFD but proved to be very promising in predicting the overall duct temperature.

In addition to the aforementioned applications for specific reactors, efforts have also been made to develop more generic 3-D reactor thermal hydraulic analysis tools based on the concept of porous media. Fiorina et al. (2015) developed a multi-scale multi-physics reactor analysis tool named GeN-Foam based on the open source Finite Volume (FV) code OpenFOAM (Greenshields, 2015). The thermal hydraulic solution of GeN-Foam combines both a traditional Reynolds Averaged Navier-Stokes (RANS) model and a porous media model on the same mesh. Such a treatment allows the equations to revert back to standard RANS equations for clear fluid, which therefore alleviates the numerical issues in case of coupled modelling using both approaches in a single simulation. Similar advantages were observed in CEA's thermal hydraulic analysis tool PolyMAC which was developed by "re-implementing" a sub-channel code within an existing CFD platform (Gerschenfeld et al., 2019). In a PolyMAC reactor model, the porous media representation of the fuel assemblies is applied together with relevant sub-channel correlations in the core sub-domain while other RANS models are applied in the surrounding CFD sub-domain. The third example is KAERI's FV code CUPID (Yoon

et al., 2017) which is developed targeting for sub-channel scale whole core analysis of PWR type reactors. The code is based on a two-phase two fluid model with consideration of the volume porosity and face permeability during the FV integration of the conservation equations. Similar to PolyMAC, CUPID can also be considered as a re-implementation of the traditional sub-channel analysis approaches in a 3-D framework.

Unlike the method used in the above examples that all solid structures (including the fuel pins and other supporting structures) are described using porosities, Viellieber and Class (2012) integrated an anisotropic porous media model in their so-called Coarse-Grid CFD (CG-CFD) to simulate a fuel assembly with supporting spacer grids, where the fuel pins are resolved using a very coarse mesh whilst the spacers that cannot be explicitly meshed are described using cell-based volume porosities and face permeabilities. Similar approach can be found in the recent work of Mikuž and Roelofs (2020) who employed a localised porous media model combined with a non-uniform momentum source term to mimic the effects of the mixing-vane spacers in their low resolution CFD model of a PWR fuel assembly. These examples show that the porous media method can be used flexibly in the simplification of the reactor core modelling. It can be used either to describe a large block of the core or to represent some sub-scale structures, depending on the desired degree of approximation for the solids.

The work presented in this paper aims to develop methodologies to couple SubChCFD and the porous media approach so as to improve the capability of the former in handling complex structures. The rest of the paper is organised as follows. In Section 2, two coupling strategies and the associated implementation of them are discussed in detail. In Section 3, two cases of rod bundle with complex structures are used to test and validate the new development. Comparisons are also made between the two methods for each of the cases to evaluate their respective performance and applicability. Conclusions are drawn in Section 4.

2. Methodology

2.1 SubChCFD

As explained in the introduction, SubChCFD can be seen as a modernised, CFD-based, sub-channel methodology. A dual mesh methodology is used, including, namely, (i) a filtering mesh which aligns with the mesh used in typical sub-channel codes, enabling the sub-channel-level wall friction and heat transfer calculated using existing engineering correlations, and (ii) a computing mesh, on which the full set of 3-D RANS governing equations are solved with a near wall closure method based on

calculations of step (i). Figure 1 shows an example of the dual mesh system for a PWR fuel channel, in which the computing mesh is created by subdividing a filtering mesh cell.

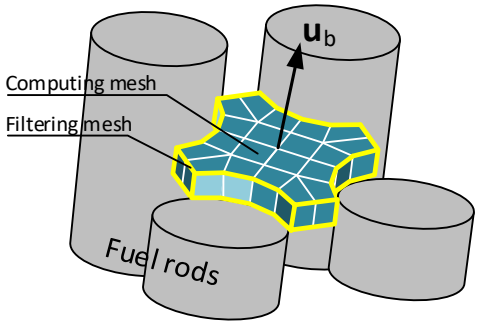

Fig. 1 Mesh system in SubChCFD

The differential forms of the RANS continuity and momentum equations for incompressible Newtonian fluids read as follows,

$$\nabla \cdot \vec{\boldsymbol{u}} = 0 \tag{1}$$

$$\rho \frac{\partial \vec{\boldsymbol{u}}}{\partial t} + \rho \nabla \cdot \left(\vec{\boldsymbol{u}} \otimes \vec{\boldsymbol{u}} \right) = -\nabla p + \nabla \cdot \bar{\bar{\sigma}} + \vec{\boldsymbol{S}}_M \tag{2}$$

where ρ is fluid density, $\vec{\boldsymbol{u}}$ is the velocity vector, t is time, p is pressure, $\bar{\bar{\sigma}}$ is the stress tensor including both the viscous and the turbulence contributions, $\vec{\boldsymbol{S}}_M$ is the body force. The computing mesh-based FV integration of the RANS momentum equation (Equation 2) with a collocated arrangement of the velocity components can be written as follows,

$$\frac{\rho V_\Omega}{\Delta t}\left(\vec{\boldsymbol{u}}^{n+1} - \vec{\boldsymbol{u}}^{n} \right) + \oint_S \vec{\boldsymbol{u}}^{n+1} \left(\vec{\boldsymbol{J}}^{n} \cdot \vec{\boldsymbol{n}} \right) dS = -\oint_S \left(\bar{\bar{I}} p \cdot \vec{\boldsymbol{n}} \right) dS + \oint_S \left(\bar{\bar{\sigma}}^{n+1} \cdot \vec{\boldsymbol{n}} \right) dS + V_\Omega \vec{\boldsymbol{S}}_M^{n}, \tag{3}$$

where V_Ω is the volume of the computing mesh cell Ω, Δt is the time step size, superscript n and n+1 represent the nth and the (n+1)th time step, respectively, $\vec{\boldsymbol{J}} = \rho \vec{\boldsymbol{u}}$ represents the convective mass flux, $\vec{\boldsymbol{n}}$ is the unit normal vector of the cell surface, S is the area of the cell surface, $\bar{\bar{I}}$ is the unit tensor.

In SubChCFD, each term of Equation 3 is treated no differently from a standard FV approach except for the diffusion term which may be the main source of error when a coarse grid is used to simulate the wall bounded shear flows. It is further decomposed into an interior part and a wall boundary part for a special treatment:

$$\oint_S \bar{\bar{\sigma}} \cdot \vec{\boldsymbol{n}} dS = \int_{S_w} \bar{\bar{\sigma}} \cdot \vec{\boldsymbol{n}} dS + \int_{S_f} \bar{\bar{\sigma}} \cdot \vec{\boldsymbol{n}} dS \,, \tag{4}$$

where S_w represents the cell surfaces adjacent to a wall boundary, and S_f the interior cell surfaces. The interior part in Equation 4 is expanded further as follows,

$$\int_{S_f} \bar{\bar{\sigma}} \cdot \vec{\boldsymbol{n}} dS = \int_{S_f} \left(\mu + \mu_t\right) \left[\nabla \vec{\boldsymbol{u}} + \left(\nabla \vec{\boldsymbol{u}}\right)^{\mathrm{T}} - \frac{2}{3} \delta \nabla \cdot \vec{\boldsymbol{u}} \right] \cdot \vec{\boldsymbol{n}} dS \,, \tag{5}$$

where the eddy viscosity μ_t is modelled using appropriate first order moment closure turbulence models. The wall boundary part, however, is calculated using the following equation:

$$\int_{S_w} \bar{\bar{\sigma}} \cdot \vec{\boldsymbol{n}} dS = -\frac{1}{4} f \frac{1}{2} \rho_{sub} \vec{\boldsymbol{u}}_{\boldsymbol{sub}} \left| \vec{\boldsymbol{u}}_{\boldsymbol{sub}} \right| \int_{S_w} dS \,, \tag{6}$$

where f denotes the skin frictional factor calculated using relevant sub-channel friction correlations, depending on the specific configurations of the fuel assembly simulated, ρ_{sub} and $\vec{\boldsymbol{u}}_{\boldsymbol{sub}}$ are the sub-channel bulk density and bulk velocity derived by averaging the CFD solutions over the corresponding filtering mesh cells, respectively.

2.2 Macroscopic governing equations

The governing equations for the flow in porous media can be derived by applying a spatial averaging operator to the standard RANS continuity equation (Equation 1) and momentum equation (Equation 2) (Vafai, 2015). The resulting equations are written as follows,

$$\nabla \cdot \left(\gamma_V \left\langle \vec{\boldsymbol{u}} \right\rangle \right) = 0 \tag{7}$$

$$\rho \frac{\partial \left(\gamma_V \left\langle \vec{\boldsymbol{u}} \right\rangle \right)}{\partial t} + \rho \nabla \cdot \left(\gamma_V \left\langle \vec{\boldsymbol{u}} \right\rangle \otimes \left\langle \vec{\boldsymbol{u}} \right\rangle \right) = -\gamma_V \nabla \left\langle p \right\rangle + \nabla \cdot \left(\gamma_V \left\langle \bar{\bar{\sigma}} \right\rangle \right) + \gamma_V \left\langle \vec{\boldsymbol{S}}_M \right\rangle + \gamma_V \vec{\boldsymbol{R}} \,, \tag{8}$$

where γ_V is the volume porosity, representing the ratio of the volume occupied by the fluid and the total volume of the averaging operator:

$$\gamma_V = \frac{V_f}{V} \,. \tag{9}$$

$\vec{\boldsymbol{R}}$ is an unknown momentum source term that appears during the averaging procedure, accounting for all resistance forces exerted by the sub-scale solid structures on the fluid. A closure modelling is

normally required to determine this term by relating it to the local macroscopic flow quantities. Symbols within the angle bracket represent the intrinsic average of the corresponding fluid quantities. The intrinsic average of a variable ϕ is defined as follows,

$$\langle \phi \rangle = \frac{1}{V_f} \int_{V_f} \phi dV \ . \tag{10}$$

It can be observed that the macroscopic governing equations (Equations 7 and 8) closely resemble the original RANS equations (Equations 1 and 2), although the physical meaning of the unknowns are different. For a clear fluid (i.e. the volume porosity is 1.0), the macroscopic governing equations automatically revert back to the standard RANS governing equations when the spatial average is performed over infinitesimal volumes.

2.3 Implementation in SubChCFD

2.3.1 Method I - embedding

The embedding method is similar to the approaches of Viellieber and Class (2012) and Mikuž and Roelofs (2020), in which a coarse-grid baseline model is created covering the entire flow domain to explicitly resolve the main geometries, whilst porous media sub-models are embedded into the baseline model to account for any other sub-scale fine structures that are difficult to be resolved using a coarse mesh. Hence, the embedding method is particularly suitable for fuel assemblies with attached fine structures that result in no significant changes to the basic sub-channel geometries. This situation appears very often in nuclear reactors, such as for the spacers grids used in fuel elements to keep fuel in place and for mixing and heat transfer enhancement. In this method, SubChCFD is applied to cover the entire domain. For the regions where the aforementioned fine structures appear, volume porosity and relevant resistance model are used to describe the reduction in area of the flow passages and the additional pressure drop caused. The equation system to be solved in the embedding method can be derived directly by implementing spatial average to the FV discretised governing equations of SubChCFD. To ensure the obtained equations to revert back to those of the original SubChCFD in case of clear fluid, the control volumes of the computing mesh are used directly as the averaging operators. Taking the momentum equation (Equation 3) as example, such a spatial averaging leads to the following equation,

$$\begin{aligned}&\frac{\rho\gamma_V V_\Omega}{\Delta t}\left(\left\langle\vec{\boldsymbol{u}}^{n+1}\right\rangle-\left\langle\vec{\boldsymbol{u}}^{n}\right\rangle\right)+\oint_S\gamma_V\left\langle\vec{\boldsymbol{u}}^{n+1}\right\rangle\left(\left\langle\vec{\boldsymbol{J}}^{n}\right\rangle\cdot\vec{\boldsymbol{n}}\right)dS\\&=-\oint_S\gamma_V\left(\overline{\overline{I}}\left\langle p\right\rangle\cdot\vec{\boldsymbol{n}}\right)dS+\oint_S\gamma_V\left(\left\langle\overline{\overline{\sigma}}^{n+1}\right\rangle\cdot\vec{\boldsymbol{n}}\right)dS+\gamma_V V_\Omega\left\langle\vec{\boldsymbol{S}}_M^{n}\right\rangle+\gamma_V\vec{\boldsymbol{R}}\end{aligned}\quad(11)$$

In a FV approach, all flow quantities are considered evenly distributed within the control volumes, so the intrinsic average of them (symbols in angle brackets in Equation 11) holds the following relation,

$$\left\langle\phi\right\rangle=\frac{1}{V_{\Omega_f}}\int_{\Omega_f}\phi dV=\phi\quad(12)$$

where ϕ denotes the flow quantities, such as $\vec{\boldsymbol{u}}$, and p. As such, Equation 11 is identical to Equation 3 for any control volumes that lie in the clear fluid region (i.e. γ_V=1 and $\vec{\boldsymbol{R}}$=0). In practice, it is not necessary to calculate the volume porosities based on the computing mesh cells, as this may lead to drastic spatial variations in the case that the sub-scale structures and the mesh cells have comparable sizes, which may potentially cause numerical issues. Instead, they are assumed to be uniformly distributed within sub-channels and can be calculated as illustrated in Figure 2. To be consistent, the resistance term in Equation 11 is also modelled based on sub-channels. This does not cause any accuracy issues, as the porous media approach is not designed to capture the details of these sub-scale fine structures, but to account for the correct overall effects with appropriate degree of approximation for them.

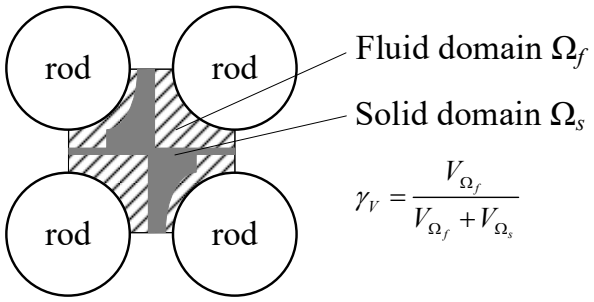

Fig. 2 Sub-channel based volume porosity calculation in the embedding method

2.3.2 Method II - interfacing

The interfacing method is perhaps a more general method than the embedding method, as there are no special requirements on the geometry of the solid structures which are to be approximated using porous media. It is particularly suitable for cases where part of the flow domain is difficult to be

handled using a body-fitted coarse-grid SubChCFD mesh, as for example in the case of the atypical structures caused by severely damaged fuels (Chinembiri et al., 2019). In such a case, an independent porous media sub-domain can be created for the block(s) with atypical structures and interfaced to the rest of the domain that is modelled by SubChCFD. In the interfacing method, the dual mesh system of SubChCFD only covers the regions that are not modelled by porous media and separate meshes are created for the porous media sub-domains. Since no solids are explicitly resolved, simple Cartesian meshes can be used for these porous media sub-domains. The whole computational domain is formed by inter connecting the porous media and the SubChCFD sub-domains through interfaces. Similar approaches can be found in many studies reported in the literature, especially those where core-scale modelling are performed (Brewster et al., 2017; Chen et al., 2017). In these studies, the porous media method is used to simplify the fuel assemblies in the core partly or entirely and the surrounding domains are usually modelled using conventional CFD. Generally, cases that are suitable for the embedding method can also be easily handled using the interfacing method. The schematic in Figure 3 clearly illustrates the basic difference between the two methods in dealing with rod bundle configurations equipped with complex sub-scale structures.

Based on the aforementioned explanation, it is clear that two governing equation systems with respective closure modelling methods are to be solved for the two sub-domains in the interfacing method. To be specific, Equations 1 and 2 are solved with the closure modelling method (Equation 6) for the SubChCFD sub-domains, whilst Equations 7 and 8 are solved with appropriate models of $\vec{\boldsymbol{R}}$ for the porous media sub-domains. Although the two equation systems deal with different types of the unknowns, they are similar in mathematical form and the solution process can be organised into a single simulation through switching between two sets of linear equation coefficients, depending on whether the local values of the volume porosities equal 1 or not. Actually, in most of the recognised CFD packages (including Code_Saturne where SubChCFD is currently implemented), porosity has been considered in formulating the equation systems. The only thing left is to properly glue the meshes of the sub-domains, which may result in non-conformal interfaces due to the difference in mesh types. In this paper, an in-built conformal mesh joining technique is used to avoid any non-conformality issues. Details can be found in (EDF R&D, 2019).

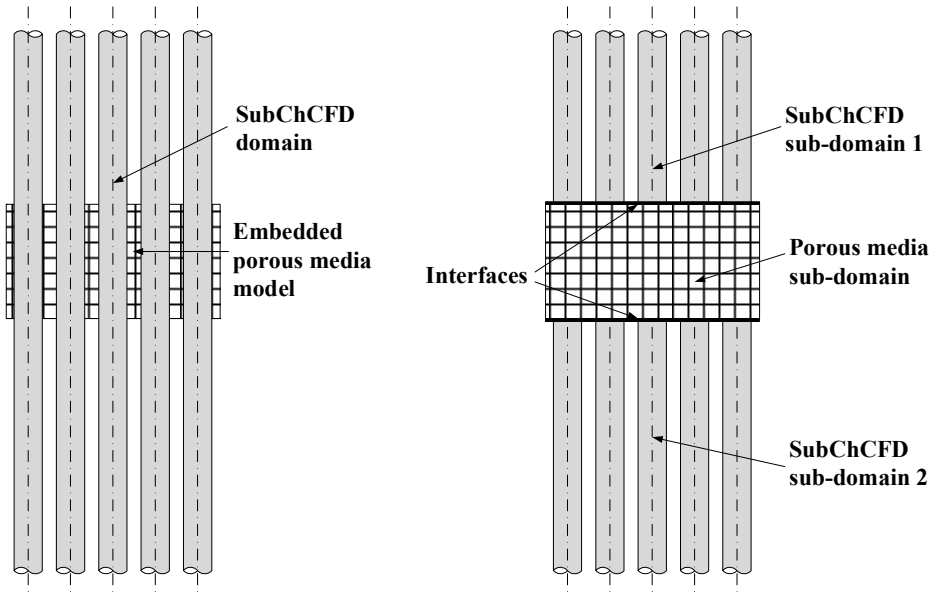

(a) (b)

Fig. 3 Application of the embedding (a) and the interfacing method (b) in rod bundle configurations equipped with sub-scale fine structures

3. Validation and Application

Two rod bundle cases are selected to test the methods described in Section 2. Both the embedding and the interfacing methods are implemented for each of the cases and comparisons are made between them to further evaluate their performance and applicability. The first case is taken from the work carried out by Creer and co-workers (Creer et al., 1979) who studied the turbulent flow near postulated sleeve blockages in a 7×7 model nuclear fuel rod bundle. The blockages are characteristic of fuel clad thermal "ballooning" which could occur during a Loss of Coolant Accident (LOCA) of a PWR, resulting in local geometrical distortion of the sub-channels. This poses challenges to SubChCFD in terms of mesh generation and closure modelling. In our recent work (Liu et al., 2020), a solution was developed to tackle such difficulties through coupling SubChCFD with an resolved CFD sub-model at the location where the blockage occurs to locally improve the prediction. The method was successful, but the computing cost was increased due to the use of an additional fine mesh and the mesh generation for the coupling was also onerous. The methods proposed in this paper for coupling porous media approach and SubChCFD are for a different purpose from that of Liu et al. (2020). In this work, we aim to simplify the modelling of complex local geometry/flow structures, and focus on producing globally accurate predictions for some key flow parameters.

The second case is taken from the joint CEA-EDF-EPRI experimental program NESTOR (Bergeron et al., 2007), in which 5×5 test rod bundles mimicking the PWR fuel assembly were used to produce high fidelity thermal hydraulic data at actual reactor operating conditions. The data were also used in the EPRI round robin benchmarking exercise (Kang and Hassan, 2016) where CFD simulations of various participants were compared and analysed for better practice of CFD in rod bundle problems. Two designs of spacer grids were investigated in the NESTOR experiment, including a simple support grid and a mixing vane grid. Such configurations are, in general, not well handled using the baseline SubChCFD models due to the challenges posed by the sub-scale fine structures (namely the spacer grids here) that cannot be directly resolved using the coarse grid. By coupling with the porous media approach, some of the main effects of the sub-scale structures on the flow, such as the local acceleration and the spacer-related head losses can be captured. Again, this method is not designed to produce detailed predictions of the flow, but to correctly capture the overall behaviour of the flow in the rod bundle configurations. For the sake of simplicity, only the case with simple support grid is considered in this test.

3.1 Flow in a 7×7 rod bundle with local fuel rod ballooning

3.1.1 Embedding method

In Creer's experiment, the rod bundle was unheated and the postulated ballooning happened at a certain height on the central nine rods, resulting in a maximum of 70% area reduction of the centre four sub-channels. Water at 29.4 °C was used as the working fluid, which entered the rod bundle from the bottom and flowed ascendingly at a bulk velocity of w_0=1.74 m/s, corresponding to a Reynolds number of 2.9×10^4 based on the hydraulic diameter of the non-damaged rod bundle geometry.

Taking advantage of the symmetries of the configuration, a numerical model is created based on ¼ sector of the entire rod bundle to save computing cost in the current study. Figure 4 shows some important geometrical details of the computational domain, in which the shaded areas represent the "extra" solids associated with the ballooning of the fuel rods. In the embedding method, these "extra" solids are treated as attached structures of an un-deformed rod bundle and not meshed explicitly. Instead, they are modelled using porous media. Consequently, the generation of the coarse mesh is greatly simplified. Figure 5a shows the main part of the mesh used in the embedding method. To better evaluate the method, numerical simulation is also performed using the baseline SubChCFD, in which the deformation of the fuel rods is directly resolved using a body-fitted coarse mesh. In addition, a

resolved CFD model is also created to provide reference results. Figures 5b and 5c show the meshes used for the two models, respectively.

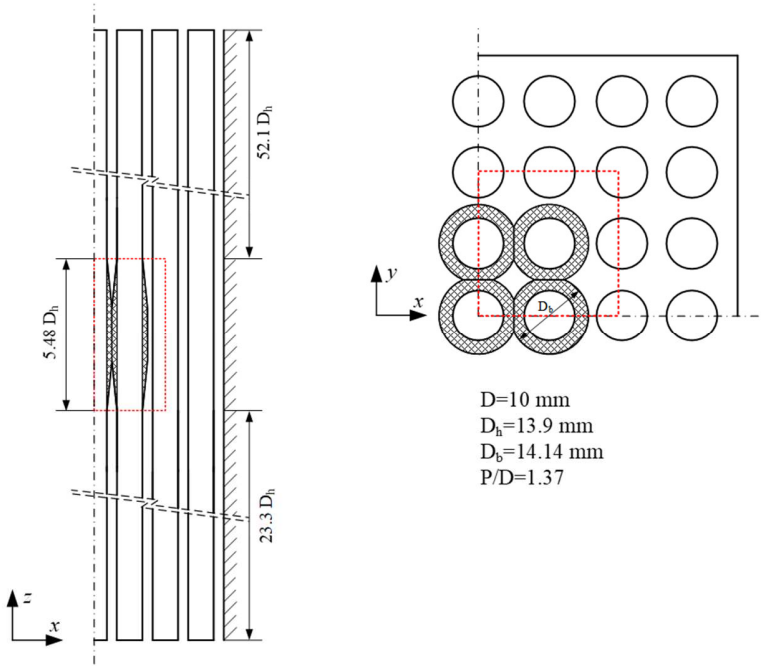

Fig. 4 Geometrical details of ¼ sector of the locally ballooned 7×7 rod bundle. The shaded areas are the "extra" solids associated with fuel rod ballooning. The red dash-line rectangles highlight the location where the embedded porous media sub-model is applied.

A non-uniformly distributed volume porosity is used to approximate the "extra" solids in the rod bundle. An in-situ calculation method is implemented at the pre-processing stage of the simulation to impose the porosity values for the computing mesh cells. An auxiliary tetrahedral mesh is created for the "extra" solids to allow the calculation to be performed numerically based on the following discrete form of Equation 9,

$$\gamma_{V,i} = 1 - \frac{\sum_{\Omega_{s,j} \subset \Omega_{ref,i}} V_{s,j}}{V_{ref,i}}, \tag{13}$$

where the summation in the numerator of the last term gives the total volume of the "extra" solids that lie within a reference filter block $\Omega_{ref,i}$ whose volume is $V_{ref,i}$. In practice, the reference filter block can be either a filtering mesh cell or a computing mesh cell, depending on the degree that the geometry

is approximated. Figure 6 shows the auxiliary mesh for the "extra" solids and the two calculation methods for the volume porosity, namely, the sub-channel based (i.e. filtering mesh-based) and the cell-based (i.e. computing mesh-based) methods. Figure 7 shows the distributions of the calculated volume porosities, which reasonably capture the geometrical features of the ballooning. It can be seen that the lowest porosity values, representing the most severe blockage to the flow passages, happen in the middle of the ballooning where the fuel rods are in contact with each other. The blockage gradually diminishes towards the two ends of the ballooning as the volume porosities increase until reaching the value of 1 where the ballooning vanishes. Compared with the sub-channel based porosity, the cell based porosity approximates the original geometry more closely but, it also varies more drastically. This, in theory, may lead to potential numerical instabilities, but we have not observed this in the current simulations. In this study, the two different calculation methods of the volume porosity lead to very similar simulation results and those produced using the sub-channel based volume porosity are presented throughout this paper.

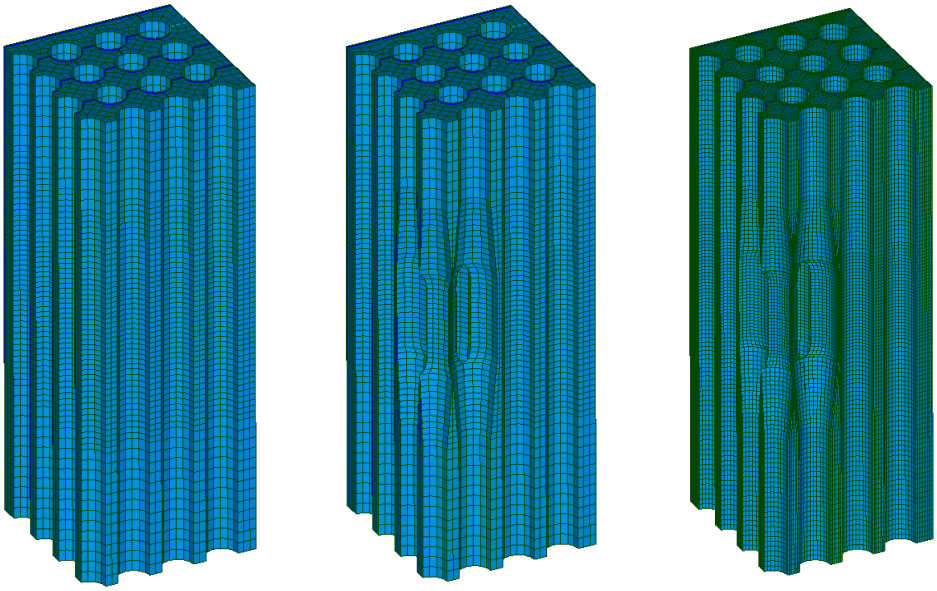

(a) (b) (c)

Fig. 5 Meshes used for the numerical models of the locally ballooned 7×7 rod bundle: the coarse mesh for the un-deformed rod bundle used in SubChCFD with embedded porous media method (a), the coarse mesh for the deformed rod bundle used in baseline SubChCFD (b), and the fine mesh for the deformed rod bundle used in resolved reference CFD

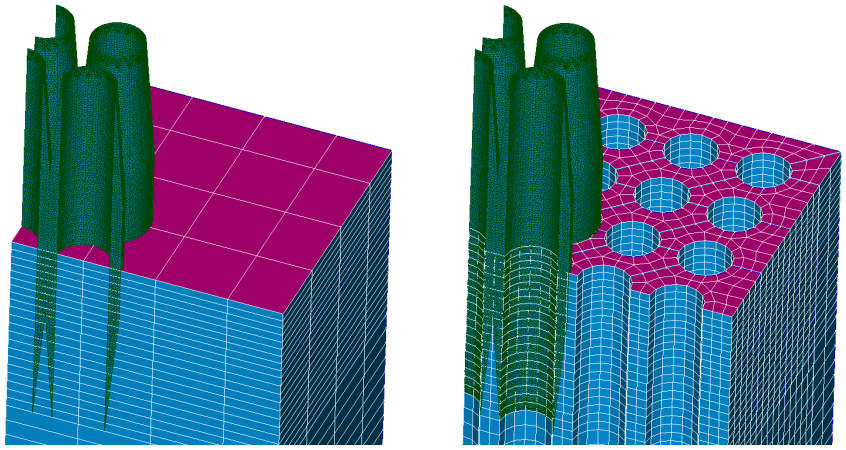

(a) (b)

Fig. 6 In-situ porosity calculation in the embedding method: the filtering mesh based (a) and the computing mesh based (b). The auxiliary mesh for the "extra" solids is shown in the horizontally clipped filtering mesh and computing mesh.

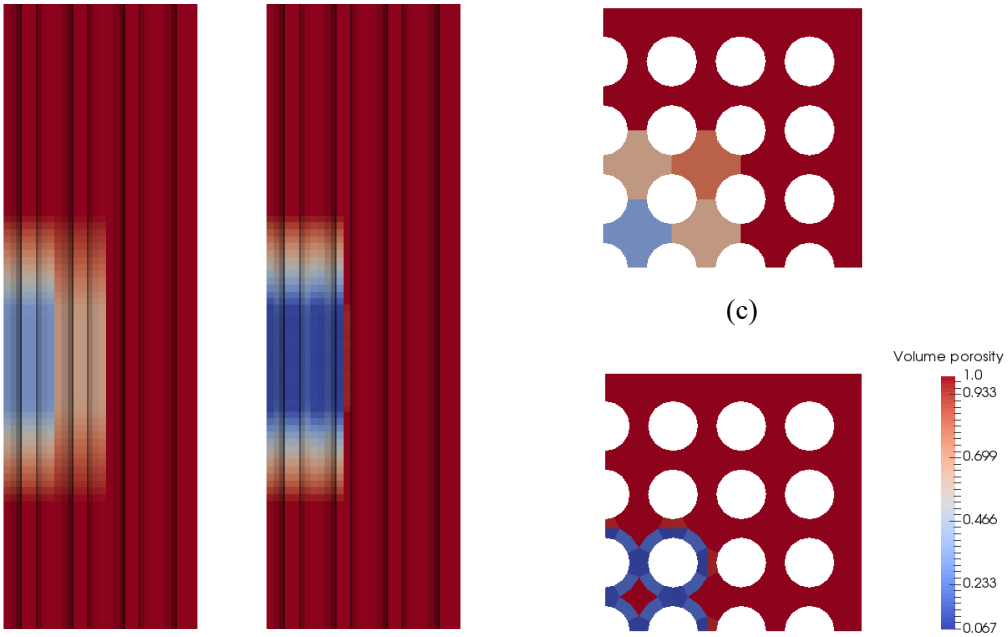

(a) (b) (c) (d)

Fig. 7 Volume porosity distributions of the locally ballooned 7×7 rod bundle in the embedding method. Side views are on the left showing the distributions of the sub-channel based (a) and the computing mesh based (b) volume porosities. Cross-sectional views are on the right showing the distributions of the sub-channel based (c) and the computing mesh based (d) volume porosities.

In the embedding method, filtering mesh cells with the volume porosities lower than 1 are marked as the porous media zone where the resistance force $\vec{\boldsymbol{R}}$ in Equation 8 needs to be specified. $\vec{\boldsymbol{R}}$ can be characterised by the pressure drop of the flow passing through the blockage, which consists of contributions of the skin friction and the form drag. Therefore, $\vec{\boldsymbol{R}}$ can be written as follows,

$$\vec{\boldsymbol{R}} = \vec{\boldsymbol{R}}_{friction} + \vec{\boldsymbol{R}}_{drag} . \tag{14}$$

The skin-friction-related resistance force $\vec{\boldsymbol{R}}_{friction}$ can be calculated using the following relation,

$$\vec{\boldsymbol{R}}_{friction} = -\frac{1}{2}\frac{\rho_{sub} f \cdot w_{sub} \left| w_{sub} \right|}{D_h}, \tag{15}$$

where f is the frictional factor, w is the axial velocity component, D_h is the hydraulic diameter, subscript "*sub*" represent the relevant quantity is sub-channel averaged. Suitable correlations are selected in line with the actual geometry of the deformed rod bundle to calculate the frictional factor f in Equation 15. For regions where the fuel rods are not in full contact, the sub-channel geometry still remains and the correlation for bare bundle in square array is used (Todreas and Kazimi, 1990), which is the same as that for the frictional factor in Equation 6. However, for regions where the fuel rods are in full contact, the correlation for the circular pipe with equal hydraulic diameter is used (Todreas and Kazimi, 1990), considering that the sub-channels turn into closed ducts under such conditions. It should be pointed out that the closure method for the SubChCFD baseline model is omitted in the porous media zone and the right hand side of Equation 6 is set to zero to avoid a double counting of the wall friction.

The form-drag-related resistance force $\vec{\boldsymbol{R}}_{drag}$ is the direct result of the blockage effect caused by the fuel rod ballooning and can be approximated using a combined head loss of a sudden contraction and a sudden expansion that happen in rod bundle configurations. Hence, it is written as follows,

$$\vec{\boldsymbol{R}}_{drag} = \frac{\Delta p_1 + \Delta p_2}{L}, \tag{16}$$

where Δp_1 and Δp_2 are pressure losses due to contraction and expansion, respectively, and L is the total length of the blockage (see Figure 8). Δp_1 and Δp_2 can be further calculated using the following relations,

$$\Delta p_1 = -\frac{1}{2}\rho K_c (w_0 \cdot |w_0|) \tag{17}$$

$$\Delta p_2 = -\frac{1}{2}\rho K_e (w_0 \cdot |w_0|), \tag{18}$$

where K_c and K_e are form loss coefficients corresponding to contraction and expansion, respectively, w_0 is a reference velocity (which is the bulk velocity at a cross-section away from the blockage in this case). Based on the geometry of the rod bundle in question, K_c takes a value of 0.4 and K_e takes a value of 0.5 (Rohsenow and Hartnett, 1998).

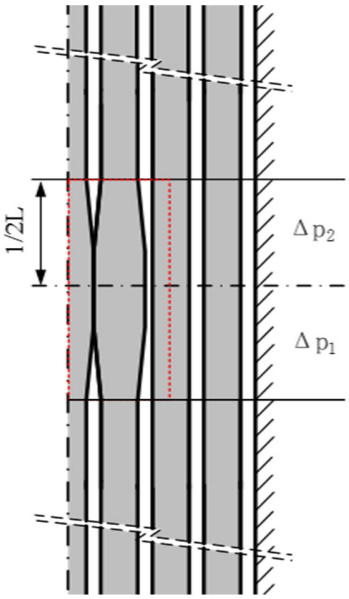

Fig. 8 Pressure losses due to the form drag

Figure 9 shows the simulation results of the sub-channel averaged velocity and pressure along the centre line of the central blocked sub-channel, where the flow is expected to be complex and difficult to predict. The results of the baseline SubChCFD model in which the blockage is explicitly resolved using the coarse mesh shown in Figure 5b is also plotted for comparison. It can be seen that the prediction of the sub-channel averaged velocity is significantly improved by using the embedding porous media method, especially in the regions downstream of the blockage. It follows the reference result much more closely than that of the baseline SubChCFD model which tends to under-predict the inter-channel mixing and result in lower axial velocities in the wake. The overall pressure drop is also well predicted compared with the reference result (see Figure 9b), although the detailed variation of

pressure across the blockage is not captured. The latter is not a concern because the method is not designed for such purposes.

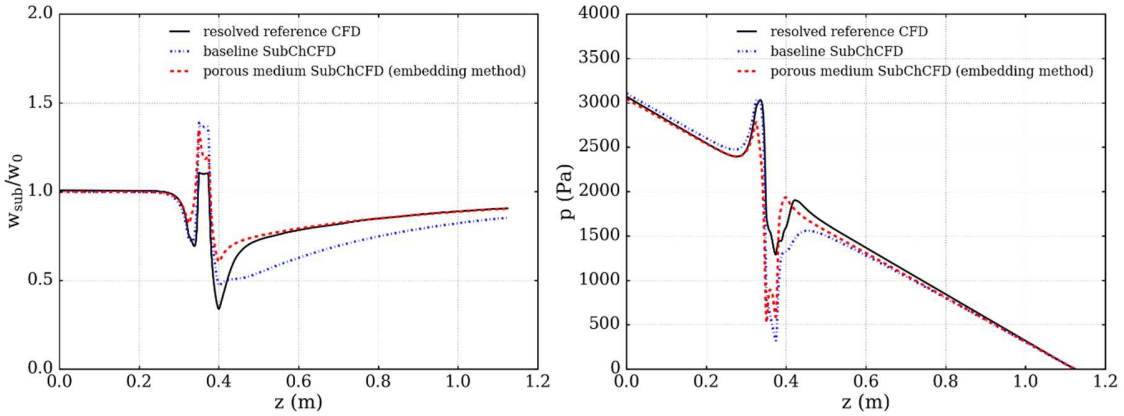

(a) (b)

Fig. 9 Comparisons of the simulation results between the porous medium SubChCFD (embedding method) and the baseline SubChCFD in the 7×7 locally ballooned rod bundle case. The sub-channel averaged axial velocity normalised by the bulk velocity (a) and the pressure (b) are plotted along the centre line of the central blocked sub-channel.

3.1.2 Interfacing method

Compared with the embedding method, it is more straightforward for the interfacing method to be applied in this case, as it is no longer necessary to decompose the ballooned fuel rods into the undeformed part and the "extra" solids to artificially ensure the existence of a regular sub-channel geometry across the blockage region. Instead, the entire region is approximated using porous media, without the need of SubChCFD model for this particular region. The SubChCFD mesh is created to cover the flow domain in the rod bundle with this region excluded (shown in Figure 10a). Meanwhile, a Cartesian mesh with a comparable grid resolution is created for the porous media sub-domain. The two meshes are then joined together at the interfaces using a conformal mesh joining technique to finally obtain the mesh for the simulation (shown in Figure 10b).

Figure 10c shows a non-uniformly distributed volume porosity in the porous media sub-domain calculated based on the local geometry. The reference filter blocks selected to perform the calculation align with the sub-channel divisions and have a reasonable resolution in the axial direction to allow some geometrical features of the blockage to be well captured. However, it is worth pointing out that using a non-uniform volume porosity does not necessarily lead to better predictions. A constant

volume porosity may be sufficient in many cases to ensure a correct overall flow and pressure drop across the porous media zone.

The resistance force $\vec{\boldsymbol{R}}$ is calculated similarly as that in the embedding method, using Equations 14 - 18. The only difference is that the sub-channel averaged axial velocity w_{sub} in Equation 15 is replaced by the filter block averaged axial velocity w_{av} in the calculation of the skin friction. In addition, the special treatment for the closure equation (Equation 6) is not required in the interfacing method, as the SubChCFD model is not applied to the porous media sub-domain.

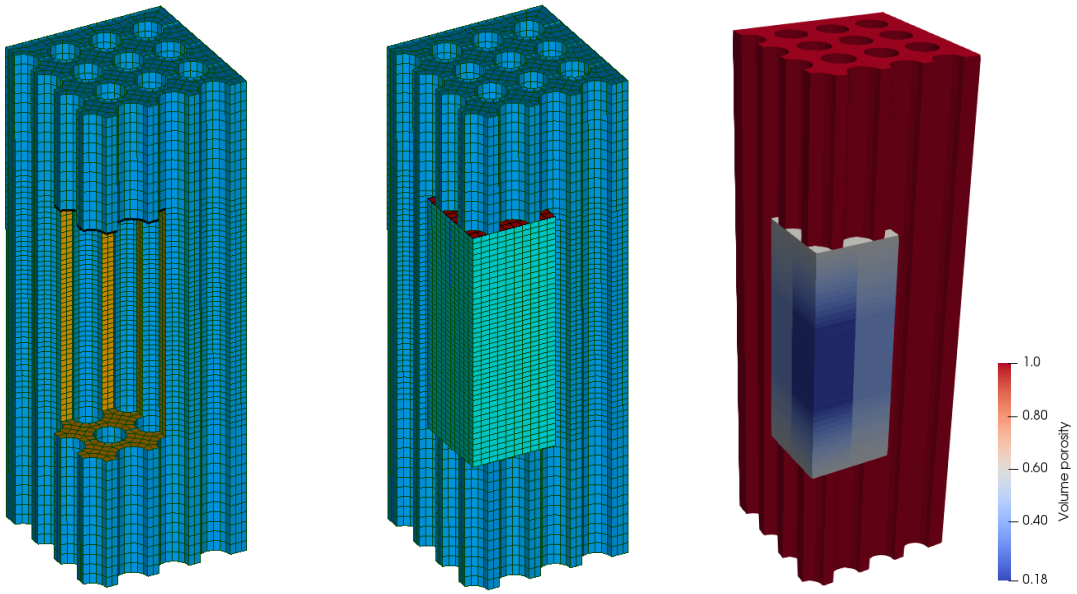

(a) (b) (c)

Fig. 10 Meshes used in the interfacing method, including a body-fitted coarse mesh for the SubChCFD sub-domain (a) and the final mesh consisting of a Cartesian mesh for the porous media sub-domain and the SubChCFD mesh (b), and the volume porosity distribution in the porous media sub-domain (c)

Figure 11 shows the simulations results that are presented in a similar way as that in Figure 9. The results produced in the embedding method are also plotted for comparison. It can be seen that the sub-channel/filter block averaged axial velocity (note that the sub-channel averaged quantities are available in the SubChCFD sub-domain and the filter block averaged quantities are available in the porous media sub-domain) in the interfacing method follows closely that of the embedding method, despite some oscillations observed at the mesh joining interfaces (see Figure 11a). This suggests that the two coupling methods of the porous media approach are, to some extent, equivalent to each other.

The oscillation at the interface is suspected to be a numerical artefact which is likely to be related to the drastic change in mesh shape and/or volume porosity and can be removed by appropriate numerical treatments. These oscillations have not produced any numerical instability or resulted in significant downstream effects in the current simulation. Additionally, the sudden change in area of the flow passages at the interfaces creates an artificial contracting or expanding flow, and thus an additional form loss. As a consequence, the overall pressure drop is slightly over-predicted compared with that of the embedding method (Figure 11b), even though the pressure loss coefficients used in the resistance force calculations are exactly the same. The over-prediction could be very severe in cases where the artificial contraction or expansion plays a big role, and consequently, a calibration for the pressure loss coefficients should be in place to offset the over-prediction.

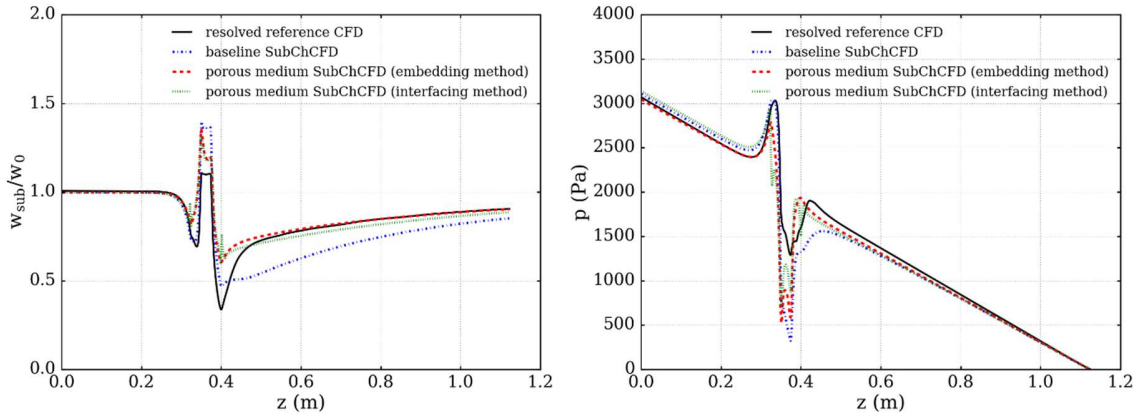

(a) (b)

Fig. 11 Comparisons of the simulation results between the porous media SubChCFD (interfacing method) and the baseline SubChCFD in the 7×7 locally ballooned rod bundle case. The sub-channel/filter block averaged axial velocity normalised by the bulk velocity (a) and pressure (b) are plotted along the centre line of the central blocked sub-channel.

3.2 Flow in a 5×5 rod bundle with simple support grids

For rod bundles with attached fine structures, the embedding method is most suitable and is hence selected for the numerical modelling for this case. Figure 12 shows the test section for the isothermal experiment (i.e. MANIVEL) in the NESTOR project (Bergeron et al., 2007). It consisted of a 5×5 square array of tube rods enclosed in a 66.1 mm × 66.1 mm square housing. The rod outer diameter was 9.5 ± 0.02 mm, and the array pitch and rod-to-wall gap were 12.6 mm and 3.1 mm, respectively. The rod bundle was approximately 5 metres long and equipped with simple support grids axially at

279 mm intervals. The spacer grids were 8 mm in height fabricated using 0.2 mm thick stainless steel sheets. Water at 30.4 °C was used as working fluid. The associated volumetric flow rate was 60.7 m^3/h, corresponding to a cross-sectional-averaged velocity (w_0) of 6.5 m/s. The resulting Reynolds number based on w_0 and the regular sub-channel hydraulic diameter ($D_{h,SC}$) was 96,300. LDV measurements for the velocity fields were performed at various elevations of the rod bundle within mainly 4 grid spans (Span 1a – 2b). The pressure drop per grid span was also measured using pressure taps distributed on the housing walls at 279 mm axial intervals.

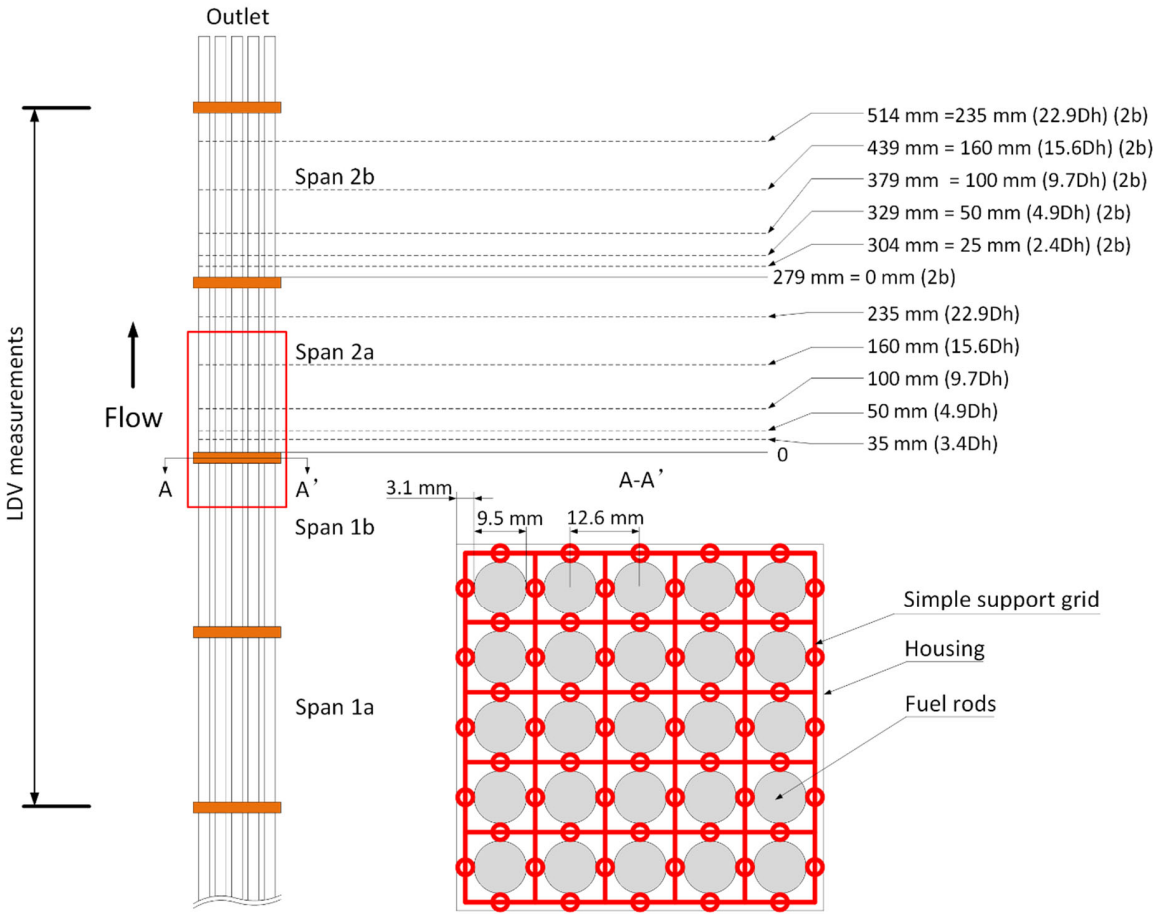

Fig. 12 Schematic of the MANIVEL simple-support-grid rod bundle in the NESTOR experiment

Considering the axial periodicity of the rod bundle configuration, a representative section of one grid span (highlighted using a red-line rectangle in Figure 12) is sufficient for the numerical modelling, provided that the flow is axially fully developed. The measuring section is located far down stream in

the rod bundle in the experiment, so it is safe to assume that the flow is fully developed there. Further, a reduction is made to the computational domain taking advantage of the cross-sectional symmetries of the rod array and the spacer grids, so that only ¼ sector of the original geometry is modelled. In the numerical model, the inlet and the outlet boundaries are treated as an identical interior surface in order to achieve the periodicity. A momentum source term is then used to drive the flow and adjusted to eventually match the target flow rate. Figure 13a shows a clipped view of the coarse-grid computing mesh used in the SubChCFD baseline model and the tetrahedral solid mesh of the simple support grid used for the in-situ porosity calculation. Figures 13b and 13c show the cross-sectional distribution of the sub-channel-based and the cell-based volume porosities, respectively. As can be seen, the former is nearly uniform across the whole cross section, whereas the latter is distributed in a "check-board" pattern. Again, the sub-channel-based volume porosity is used in the simulation for robustness.

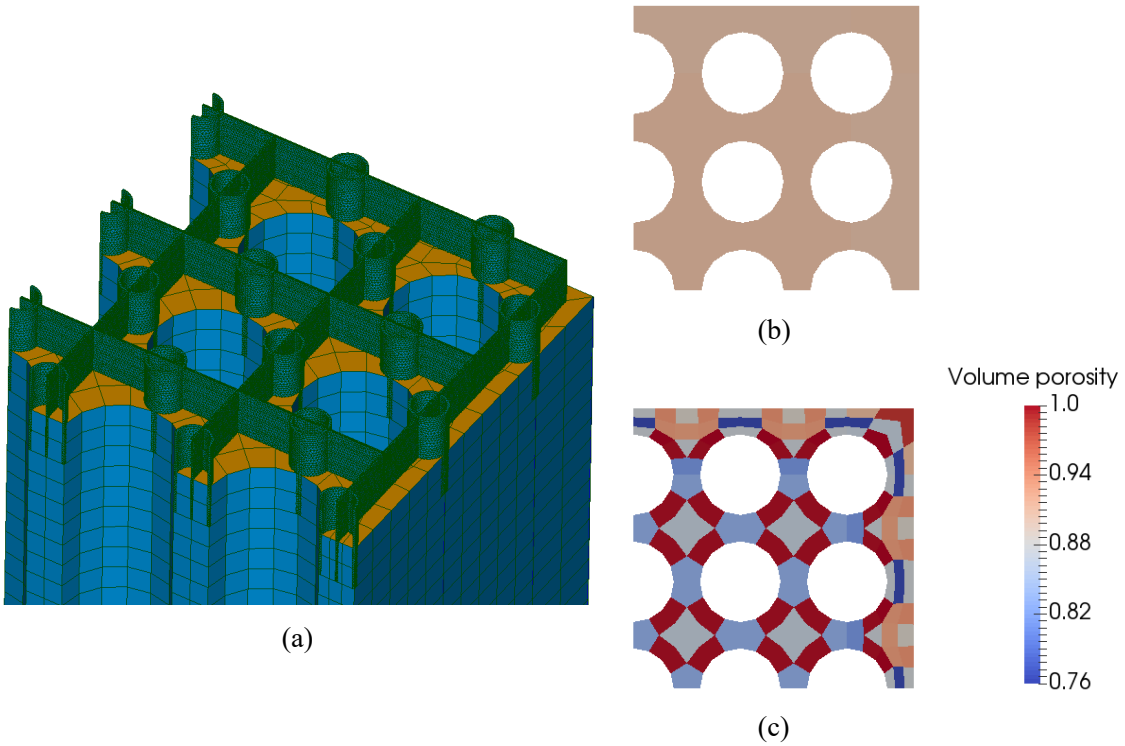

Fig. 13 Computing mesh of the SubChCFD baseline model and the solid mesh for the simple support grid used in porosity calculations (a) and the cross-sectional distributions of the sub-channel-based (b) and the cell-based (c) volume porosities

The axial pressure drop across the segment of the rod bundle equipped with the simple support grid consists of the contributions of the wall shear on the rods and the spacer-related pressure loss. The former is taken into account automatically by the SubChCFD baseline model through the closure

model (Equation 6), whereas the latter is modelled using the resistance force $\vec{\boldsymbol{R}}$ in the porous media sub-model. $\vec{\boldsymbol{R}}$ is further written in the following form,

$$\vec{\boldsymbol{R}} = \frac{\Delta P_G}{L}, \tag{19}$$

where ΔP_G is the spacer-related pressure loss, L is the longitudinal length of the spacer grid. ΔP_G includes the contributions of the skin friction exerted by the surfaces of the spacer grid and the form drag due to the obstructive effect caused by the spacer grid. Here, the two forces are modelled together and hence, ΔP_G can be calculated using a single relation as follows,

$$\Delta P_G = -\frac{1}{2}\rho K_G \left(w_0 \cdot |w_0| \right), \tag{20}$$

where K_G is the one-grid-span spacer-related pressure loss coefficient. Using the correct value of K_G is crucial in achieving an accurate prediction of the pressure drop in the simulation. K_G can be obtained either through the existing drag coefficient database for spacers with similar configurations or directly extracted from the pressure drop data collected in the experiment. In this paper, the drag coefficient for the honeycomb type spacers which closely resemble the simple support grid is used to approximate K_G (Rehme, 1973). For the flow condition in question, the K_G value is about 0.42 which agrees surprisingly well with that calculated using the correlation derived by regression-fit of the experimental data,

$$K_G = 3.3424\,\mathrm{Re}_{D_h}^{-0.181} = 0.429, \tag{21}$$

where Re_{D_h} is the Reynolds number based on the hydraulic diameter (D_h) accounting for the total test section wetted perimeter and the bulk velocity w_0.

Figure 14 shows the simulated pressure variation along one grid span. Two sets of representative CFD results provided by the participants of the round robin benchmarking exercise are also plotted for comparison. They were produced by a rough wall RANS simulation using ANSYS FLUENT and a smooth wall RANS simulation using Code_Saturne, respectively. The Measured one-grid-span pressure drop is 20,000 Pa which is in good agreement with the simulation result of the embedding method, suggesting that the correlations used for fuel rod wall shear and spacer-related pressure loss are accurate and reliable. However, it is surprising that both of the CFD results under-predict the overall pressure loss, especially the one without considering the wall roughness, giving approximately

40% under-prediction as compared to the experiment. According to EPRI's report for this benchmarking exercise (EPRI, 2014), the under-prediction of the spacer-related pressure loss in the CFD simulation is the main source of the under-prediction of the total grid span pressure loss, indicating again that there is still a long way for resolved CFD to be entirely trustable in handling such complex geometries.

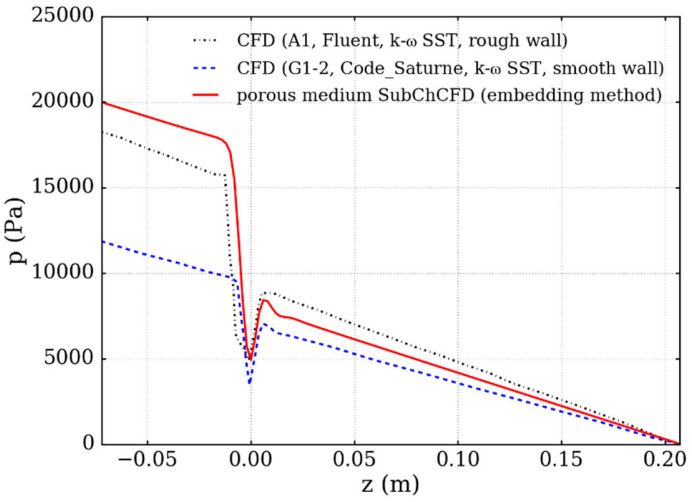

Fig. 14 Pressure variations along one grid span predicted by the porous medium SubChCFD (embedding method) and CFD simulations

The axial velocity predicted by the simulation is plotted along a lateral line (i.e. line 2 in Figure 15) at a location 35 mm ($3.4D_h$) downstream of the spacer grid to further investigate the performance of the embedding method. Experimental data are also plotted correspondingly for comparison. It can be seen in Figure 15 that the velocity profile is significantly distorted by the spacer grid as indicated by the experimental data. However, this phenomenon cannot be captured by the current implementation of porous medium SubChCFD due to the low resolution computing mesh used and the uniformly distributed resistance force across the sub-channels. The slowing-down of the flow at centres of the sub-channels can be, to some extent, predicted if a non-uniform resistance force is implemented to account for the detailed effects of the spacer grid. Despite this, the overall flow distribution is still well predicted.

Figure 16 shows the sub-channel averaged axial velocities normalised by the bulk velocity at the elevation of 235 mm which is equivalent to the axial location of 44 mm upstream of the spacer grid in the current model (see Figure 12). Three sets of representative CFD results taken from the round robin benchmarking exercise are also plotted for comparison. It can be seen that the result produced

by the embedding method agrees well with that of the CFD model G1-2 where the k-ω SST turbulence model is employed and Code_Saturne is used to perform the simulation. This suggests that the porous medium SubChCFD has a comparable performance as resolved CFD in terms of the predictions for sub-channel averaged flow quantities, but meanwhile it requires much less computing resources than the latter.

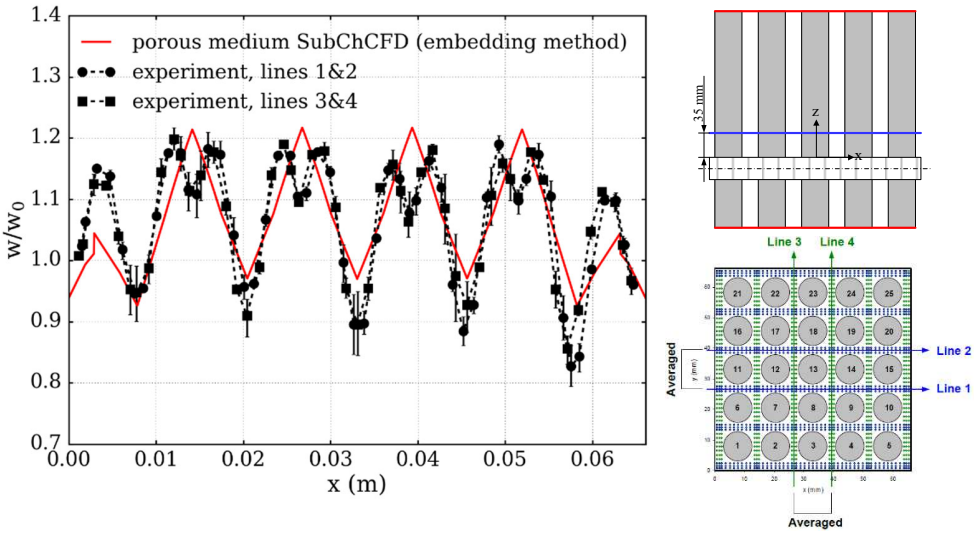

Fig. 15 Axial velocity profiles normalised by bulk velocity just downstream of the simple support grid. The axial location for the plots and the lines for averaging the experimental data are also shown.

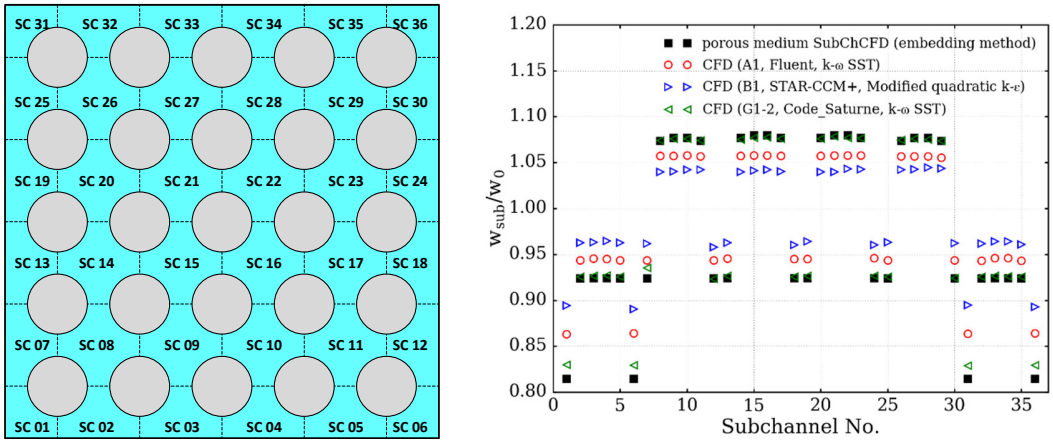

Fig. 16 Sub-channel averaged axial velocities normalised by the bulk velocity at z=235 mm

In theory, the interfacing method can also be applied to this case, despite being not as suitable as the embedding method. For completeness, numerical simulation is also performed using the interfacing method. Figure 17 shows the simulation result of the pressure variation along one grid span produced by the interfacing method. The result is also compared with that of the embedding method which has proven to be in good agreement with the experiment. It can be seen that the spacer-related pressure loss is severely over-predicted using the interfacing method, resulting in an 50% over-prediction of the one-grid-span pressure loss. This is not surprising because the artificial expansion and contraction of the flow passages that appear at the interfaces to bridge the porous media and the SubChCFD sub-domains play a significant role in this case (note that the porous media sub-domain is very short longitudinally) and result in a strong numerical "form loss" which would be too strong to be offset by calibrating the pressure loss coefficients. This suggests that the coupling method should be selected with caution in practical applications to ensure it fit well with the problem so as to achieve good predictions.

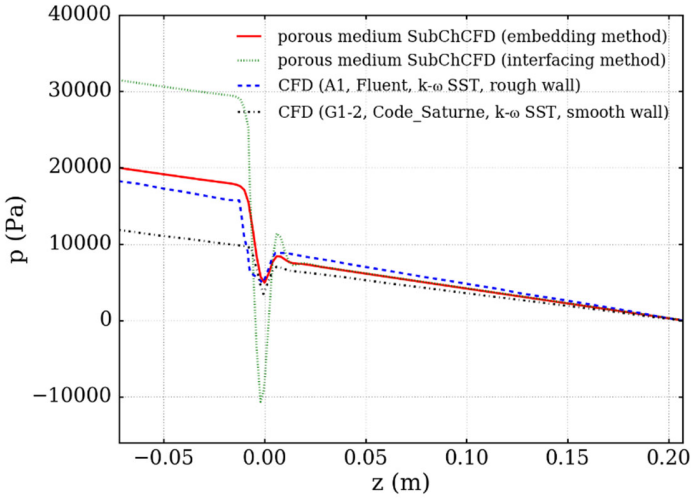

Fig. 17 Pressure variations along one grid span predicted by the porous medium SubChCFD (interfacing method) and CFD simulations

4. Conclusions

In order to expand the application of SubChCFD to fuel assemblies with complex internal structures, methods of coupling it with the porous media approach are proposed and discussed in this paper, based on embedding and interfacing. The former is designed for handling fine structures that are attached to the rod bundle but themselves do not change the basic geometry of the sub-channels in a fuel assembly.

Therefore, a SubChCFD baseline model can be created for the bare bundle geometry and porous media sub-models can be embedded in the regions where the sub-scale fine structures are located to account for the related effects of flow blockage and pressure drop.

Compared with the embedding method, the interfacing method is more general and has no special requirements on the geometry of the solid structures to be approximated. Therefore, the interfacing method can not only be used for the complex structures that are difficult to be dealt with using SubChCFD, but also to simplify some large blocks in a domain where the detailed flow features are of no interest to further reduce the computing cost. In the interfacing method, all solids (including the fuel pins) are considered in the calculation of the volume porosities, thus separate meshes need to be created for the porous media sub-domains and interfaced to the SubChCFD mesh which usually covers the rest of the whole domain.

In this paper, two rod bundle configurations are used to test and validate the coupling methods: one is a 7×7 rod bundle with locally ballooned fuel rods, and the other is a 5×5 PWR rod bundle equipped with simple support grids. For the first case, both the embedding and the interfacing methods perform well and produce satisfactory results. The predictions of the flow field downstream of the blockage are significantly improved compared with that of the baseline SubChCFD. Although small discontinuities in the flow field near the interfaces occur in the simulation result of the interfacing method, this does not significantly affect the overall picture of the prediction. In addition, the predicted global pressure drop is also accurate.

For the second case, simulation is performed first using the embedding method, because it is specifically designed to deal with such problems. The overall pressure drop across the rod bundle is predicted very accurately thanks to the use of the pressure loss coefficient of the honeycomb spacer grid which resembles the simple support grid very closely. In addition, the sub-channel averaged velocity distribution is also correctly predicted, agreeing well with one of the resolved CFD results provided by the round robin benchmarking exercise (Kang and Hassan, 2016). The interfacing method is also tested for this case, however, the simulation results obtained are not satisfactory. The grid span pressure drop is severely over-predicted, which may be attributed to the fact that the “interfacing effect” in the form of artificial expansion and contraction of the flow passages causes a big error in this case.

Nomenclature

D	Diameter of the fuel rod in a rod bundle, m
D_b	Maximum diameter of the ballooned fuel rod in the 7×7 rod bundle, m
D_h	Hydraulic diameter of a rod bundle, m

f	Skin fractional factor
$\overline{\overline{I}}$	Unit tensor
$\vec{J}$	Convective mass flux, kg/m^2·s
K_c	Coefficient of the form loss due to a sudden contraction
K_e	Coefficient of the form loss due to a sudden expansion
K_G	Spacer-related pressure loss coefficient of NESTOR MANIVEL simple support grid
L	Stream-wise length of the porous media zone, m
$\vec{n}$	Unit normal face vector of a cell face
p	Pressure, Pa
P	Pitch of a rod bundle, m
$\vec{R}$	Resistance force in porous media, N/m^3
Re	Reynolds number
$\vec{S}_M$	General source term of the momentum equation, N/m^3
S	Surface area of a cell face, m^2
S_f	Interior cell face, m^2
S_w	Wall adjacent cell face, m^2
t	Time, s
Δt	Time increment, s
$\vec{u}$	Velocity vector, m/s
V_Ω	Volume of the control volume Ω, m^3
V_f	Volume occupied by fluid in a reference domain for porosity calculation
V	Volume of a reference domain for porosity calculation
w	Axial velocity, m/s
x, y, z	Spatial coordinate, m

614 **Greek Letters**

γ_V	Volume porosity
δ	Kronecker delta
μ	Molecular viscosity, Pa·s
μ_t	Eddy viscosity in a RANS momentum equation, Pa·s
ρ	Density, kg/m^3
$\overline{\overline{\sigma}}$	Stress tensor, Pa
ϕ	General variable
Ω	Control volume in a FV approach

615 **Superscripts**

n	Time step n
$n+1$	Time step n+1

616 **Subscripts**

drag	Form drag part of the resistance force
f	Quantities for fluid
friction	Friction part of resistance force
s	Quantities for solid
sub	Sub-channel averaged quantities
0	Cross-sectional averaged quantities at a reference location

Acknowledgements

The present work was carried out as part of the R&D Program for Digital Reactor Design sponsored by the Department of Business, Energy and Industry Strategies (BEIS) of the UK (Ref 1659/10/2018). We appreciate the fruitful discussions with the project team members and are especially grateful for the useful feedbacks provided by C. Howlett and R. Underhill of Frazer-Nash Consultancy. The authors would also like to acknowledge the support received through EPSRC's Collaborative Computational Project (CCP) for nuclear thermal hydraulics (No. EP/T026685/1).

References

Ansys Inc., 2011. Ansys Fluent 14.0 User's Guide.

Bergeron, A., Chataing, T., Garnier, J., Decossin, E., Peturaud, P., Yagnik, S.K., 2007. Design, Feasibility, and Testing of Instrumented Rod Bundles to Improve Heat Transfer Knowledge in PWR Fuel Assemblies, in: Proceedings of the 2007 LWR Fuel Performance Meeting. San Francisco.

Brewster, R.A., Bissett, T.A., Xu, Y., 2017. Computational Fluid Dynamics Assessment of Baffle Plate Leakage Flow Effects in a Downflow 4-Loop Reactor, in: Proceedings of 17th International Topical Meeting on Nuclear Reactor Thermalhydraulics (NURETH-17). Xi'an.

Chandesris, M., Serre, G., Sagaut, P., 2006. A macroscopic turbulence model for flow in porous media suited for channel, pipe and rod bundle flows. Int. J. Heat Mass Transf. 49, 2739–2750. https://doi.org/10.1016/j.ijheatmasstransfer.2005.12.013

Chen, R., Tian, M., Chen, S., Tian, W., Su, G.H., Qiu, S., 2017. Three dimensional thermal hydraulic characteristic analysis of reactor core based on porous media method. Ann. Nucl. Energy 104, 178–190. https://doi.org/10.1016/j.anucene.2017.02.020

Chen, Z., Chen, X.N., Rineiski, A., Zhao, P., Chen, H., 2015. Coupling a CFD code with neutron kinetics and pin thermal models for nuclear reactor safety analyses. Ann. Nucl. Energy 83, 41–49. https://doi.org/10.1016/j.anucene.2015.03.023

Chinembiri, K., He, S., Li, J., Trinca, C., 2019. Numerical study of heat transfer in a distorted rod bundle. Nucl. Eng. Des. 349, 63–77. https://doi.org/10.1016/j.nucengdes.2019.04.003

Cong, T., Tian, W., Su, G., Qiu, S., Xie, Y., Yao, Y., 2014. Three-dimensional study on steady thermohydraulics characteristics in secondary side of steam generator. Prog. Nucl. Energy 70, 188–198. https://doi.org/10.1016/j.pnucene.2013.08.011

Creer, J.M., Bates, J.M., Sutey, A.M., 1979. Turbulent flow in a model nuclear fuel rod bundle containing partial flow blockages. Nucl. Eng. Des. 52(1), 15–33.

649 Darcy, H.P.G., 1856. Les Fontaines publiques de la ville de Dijon. Exposition et application des
650 principes à suivre et des formules à employer dans les questions de distribution d'eau, etc. V.
651 Dalamont, Paris.
652 EDF R&D, 2019. Code_Saturne version 6.0.0 practical user's guide.
653 EPRI, 2014. Computational Fluid Dynamics Benchmark of High Fidelity Rod Bundle Experiments
654 Industry Round Robin Phase 1 - Rod bundle with simple supporting grids. Palo Alto, CA.
655 Fiorina, C., Clifford, I., Aufiero, M., Mikityuk, K., 2015. GeN-Foam: A novel OpenFOAM® based
656 multi-physics solver for 2D/3D transient analysis of nuclear reactors. Nucl. Eng. Des. 294, 24–
657 37. https://doi.org/10.1016/j.nucengdes.2015.05.035
658 Gerschenfeld, A., Gorsse, Y., Fauchet, G., 2019. Development of a polyhedral staggered mesh scheme
659 application to subchannel and CFD SFR thermal-hydraulics. 18th Int. Top. Meet. Nucl. React.
660 Therm. Hydraul. NURETH 2019 3329–3342.
661 Greenshields, C.J., 2015. OpenFOAM User Guide. OpenFOAM Found. Ltd.
662 Hanna, B.N., Dinh, N.T., Youngblood, R.W., Bolotnov, I.A., 2020. Machine-learning based error
663 prediction approach for coarse-grid Computational Fluid Dynamics (CG-CFD). Prog. Nucl.
664 Energy 118, 103140. https://doi.org/10.1016/j.pnucene.2019.103140
665 Kang, S.K., Hassan, Y.A., 2016. Computational fluid dynamics (CFD) round robin benchmark for a
666 pressurized water reactor (PWR) rod bundle. Nucl. Eng. Des. 301, 204–231.
667 https://doi.org/10.1016/j.nucengdes.2016.03.007
668 Liu, B., He, S., Moulinec, C., Uribe, J., 2021. A Coupling Approach between Resolved and Coarse-
669 grid Sub-channel CFD. Nucl. Eng. Des. (accepted).
670 Liu, B., He, S., Moulinec, C., Uribe, J., 2019. Sub-channel CFD for nuclear fuel bundles. Nucl. Eng.
671 Des. 355, 110318. https://doi.org/10.1016/j.nucengdes.2019.110318
672 Mikuž, B., Roelofs, F., 2020. Low resolution modelling of mixing phenomena in PWR fuel assemblies.
673 Nucl. Eng. Des. 360, 110504. https://doi.org/10.1016/j.nucengdes.2019.110504
674 Patankar, S. V, Spalding, D.B., 1972. A Calculation Procedure for the Transient and Steady-state
675 Behaviour of Shell-and-tube Heat Exchangers, Imperial College Dept. Mechanical Engineering.
676 Imperial College of Science and Technology, Department of Mechanical Engineering.
677 Rahimi, M.H., Jahanfarnia, G., 2014. Thermal-hydraulic core analysis of the VVER-1000 reactor
678 using a porous media approach. J. Fluids Struct. 51, 85–96.
679 https://doi.org/10.1016/j.jfluidstructs.2014.08.002
680 Rehme, K., 1973. Pressure Drop Correlations for Fuel Element Spacers. Nucl. Technol. 17, 15–23.
681 https://doi.org/10.13182/NT73-A31250

682 Rohsenow, W.M., Hartnett, J.R., 1998. Handbook of heat transfer, 3rd ed, Choice Reviews Online.
683 McGraw-Hill, New York: https://doi.org/10.5860/choice.36-3347
684 Sha, W.T., Yang, C.I., Kao, T.T., Cho, S.M., 1982. Multidimensional numerical modeling of heat
685 exchangers 104.
686 Todreas, N.E., Kazimi, M.S., 1990. Nuclear Systems I: Thermal Hydraulic Fundamentals. Taylor &
687 Francis.
688 Vafai, K., 2015. Handbook of porous media, third edition, Handbook of Porous Media, Third Edition.
689 https://doi.org/10.1201/b18614
690 Vafai, K., Tien, C.L., 1981. Boundary and inertia effects on flow and heat transfer in porous media.
691 Int. J. Heat Mass Transf. 24, 195–203. https://doi.org/10.1016/0017-9310(81)90027-2
692 Viellieber, M., Class, A., 2015. Coarse-Grid-CFD for the Thermal Hydraulic Investigation of Rod-
693 Bundles. Proc. Appl. Math. Mech 15, 497–498. https://doi.org/10.1002/pamm.201510239
694 Viellieber, M., Class, A.G., 2012. Anisotropic porosity formulation of the coarse-grid-CFD (CGCFD),
695 in: Proceedings of the 2012 20th International Conference on Nuclear Engineering Collocated
696 with the ASME 2012 Power Conference ICONE20-POWER2012. California, pp. 1–11.
697 Yoon, S.J., Kim, S.B., Park, G.C., Yoon, H.Y., Cho, H.K., 2017. Application of Cupid for Subchannel-
698 Scale Thermal-Hydraulic Analysis of Pressurized Water Reactor Core Under Single-Phase
699 Conditions. Nucl. Eng. Technol. 50, 54–67. https://doi.org/10.1016/j.net.2017.09.008
700 Yu, Y., Merzari, E., Obabko, A., Thomas, J., 2015. A porous medium model for predicting the duct
701 wall temperature of sodium fast reactor fuel assembly. Nucl. Eng. Des. 295, 48–58.
702 https://doi.org/10.1016/j.nucengdes.2015.09.020
703